RSC Advances

PAPER

View Article Online
View Journal | View Issue

Cite this: *RSC Adv.*, 2025, **15**, 38603

Synergistic hydrolysis, coordination and hydrogen bond interactions in NIPS for underwater superoleophobic mesh-based oil/water separation

Yuxiang Liu,†[a] Yuchen Li,†[a] Congying He,[a] Xin Yue,[c] Shiming Hu,[a] Hongyi Wang,[a] Niaz Ali Khan,[d] Chao Yang*[b] and Mengying Long *[a]

Received 24th August 2025
Accepted 9th October 2025

DOI: 10.1039/d5ra06305a

rsc.li/rsc-advances

Constructing a durable, high-flux, and fouling-resistant coating on metal meshes without compromising their structural integrity remains a formidable challenge. Herein, we report a novel non-solvent induced phase separation (NIPS) strategy that enables the synchronous occurrence of antimony trichloride hydrolysis, metal–polyphenol coordination, and PVP–TA hydrogen bonding during membrane formation, realizing collaborative interface engineering of membrane formation and functionalization in a single step. The synergistic effect leads to the *in situ* growth of a robust superhydrophilic network on the metal mesh without destroying the substrate. The resulting membrane achieves a high flux (8000 L m^{-2} h^{-1}) under gravity, along with excellent underwater self-cleaning ability and chemical stability. This work provides an efficient, time-saving, and economical method to prepare high flux and underwater self-cleaning wire mesh oil–water separation membranes.

1. Introduction

The escalating discharge of industrial oily wastewater and frequent marine oil spills have intensified the global demand for efficient oil–water separation technologies.[1–5] Membrane-based separation has emerged as a promising strategy for oil–water separation due to its high efficiency and low energy consumption.[6–8] High flux is a key goal for industrial wastewater treatment applications where large volumes must be processed.[9,10] Metal mesh is a kind of substrate, which easily obtains high flux for oil–water separation by coating with functional materials.[11–16] Unlike pressure or electricity driven separation methods, mesh systems often operate *via* gravity to reduce energy demands,[17–19] which aligns with global efforts to develop low-carbon wastewater treatment technologies.

Metal mesh-based oil–water separation membranes are commonly fabricated by surface micro–nano structure engineering and chemical modification, achieving either superhydrophilic/underwater superhydrophobic or superhydrophobic/superoleophilic properties. The key methodologies include: chemical etching, where surface roughness is generated through etching prior to grafting low-surface-energy molecules;[21–23] electrochemical deposition,[24,25] which constructs micro–nano rough structures *via* electrolysis followed by low-surface-energy modifications to attain tailored wettability; and hydrothermal synthesis, involving high-temperature/pressure reactions to form hierarchical metal hydroxide nanostructures.[26,27] However, these methods often involve multi-step procedures and harsh conditions (*e.g.*, strong acids, high temperature) that can compromise the mechanical strength of the metallic substrate. More importantly, the pre-designed micro/nano structures and grafted molecules are susceptible to physical abrasion and chemical degradation, leading to performance failure during long-term operation. An ideal alternative should therefore allow for one-step fabrication under mild conditions, simultaneously constructing the necessary hierarchical structure and chemical functionality without damaging the substrate.

The non-solvent induced phase separation (NIPS) technology, albeit well established for high-performance polymer membranes,[28–30] remains unexplored for metal mesh modification. Its potential to orchestrate multiple reactions within a confined timeframe and space offers a unique opportunity to address the above challenges. By easily adjusting parameters of casting solution composition or coagulation bath composition, NIPS produces tailored pore sizes, porosity, and surface morphology of membranes with fewer steps, thus reducing energy and production costs. Moreover, it allows blending with nanoparticles or additives to enhance hydrophilicity, antifouling properties, or selectivity in the forming processes of membrane, leading to the forming and modifying in one

[a]College of Science, Civil Aviation University of China, Tianjin 300300, China. E-mail: longmengyingscut@163.com
[b]State Key Laboratory of Petroleum Molecular & Process Engineering, Research Institute of Petroleum Processing, SINOPEC, Beijing 100083, China
[c]College of Aeronautical Engineering, Civil Aviation University of China, Tianjin 300300, China
[d]Interdisciplinary Research Center for Membranes and Water Security, King Fahd University of Petroleum & Minerals, Dhahran 31261, Saudi Arabia
† Yuxiang Liu and Yuchen Li are co-first authors; they contributed equally to the work.

step.[31–33] To date, limited studies have been reported on fabricating metal-based oil–water separation membranes *via* the NIPS method.

Herein, we propose a facile NIPS method to fabricate mesh-based membranes with integrated high flux, underwater self-cleaning functionality, and robustness. The hydrophilic groups, such as phenolic hydroxyl, carboxyl, amido hydroxyl, and so on, are successfully loaded without destroying the metal mesh structure, and the preparation of mesh-based membrane and superhydrophilic and underwater superoleophobic modification are simultaneously realized. By strategically design the composition of the casting solution and coagulation bath, the NIPS process is utilized as a dynamic reaction platform to orchestrate three synergistic interactions in a single step: (1) $SbCl_3$ hydrolyzed into $Sb_4O_5Cl_2$; (2) the Sb^{3+} reacted with TA to form the metal–polyphenol coordination network; (3) the hydrogen bonding interaction formed between TA and PVP. The resulting membranes demonstrate optimized gravity-driven separation performance with a flux up to 8000 L m^{-2} h^{-1}. The synergy of hydrolysis, coordination, and hydrogen bonding enables the simultaneous formation of a micro/nano-porous structure and the grafting of high-density hydrophilic groups, which collaboratively give rise to an exceptionally stable hydration layer. Therefore, the membrane surface exhibits superhydrophilicity and underwater superoleophobicity, effectively preventing oil adhesion through hydration repulsion forces. Compared to conventional modification methods, our one-pot NIPS strategy eliminates post-treatment steps while leveraging low-cost precursors. This work provides fundamental insights into the simple and highly efficient preparation of metal mesh-based oil–water separation membranes.

2. Experimental details

2.1. Materials and chemicals

Poly(vinylidene fluoride) (PVDF P302014, purity over 99.0%, M_n = 130 000–150 000 Da), PVP (K30, $M_w \sim$ 40 000 Da), *N*,*N*-dimethylacetamide (DMAC, purity over 99.0%, M_w = 87.12 Da), $SbCl_3$ (purity over 99.0%, M_w = 228.12 Da), TA (purity over 99.5%, M_n = 1701.2 Da), hexane (purity over 97%, M_n = 86.175 Da), and sodium dodecyl sulfate (SDS) were purchased from Shanghai Aladdin Biochemical Technology Co., Ltd (Shanghai, China). Evans blue (M_n = 960.805) and Sudan III (purity over 99.0%, M_n = 352.39 Da) were purchased from Meryer Chemical Technology (Shanghai, China). Heptane (purity over 99.0%, M_n = 100.202) was purchased from Tianjin Guangfu Technology Development Co., Ltd Vacuum pump oil (purity over 99.0%) was purchased from ULVAC KIKO, Inc. (Japan). Silicon oil and soybean oil were purchased from Shanghai Macklin Biochemical Co., Ltd. The molecular weight, which manufactured by Tianning Meijie Wire Mesh Business Department (Jiang Su, China).

2.2. Preparation of membranes

Mesh-based oil–water separation membranes were prepared using the NIPS method. The casting solution was prepared by mixing the PVDF, PVP, $SbCl_3$ and DMAC at magnetic stirring with 700 rpm of the stirring speed at 80 °C for 4 h, and their recipe was shown in Table S1. The casting solution was degassed in the oven at 60 °C for 24 h. The wire mesh was immersing in absolute ethanol to remove organic residues under the ultrasonic for 10 min, and further washed by deionized water. The cleaned wire mesh was completely immersed in a casting solution heated to 50 °C for 3 minutes. The solution-soaked wire mesh was then completely submerged in a coagulation bath at 25 °C for 10 minutes.[30,31] The resulting membrane was washed by deionized water before performance measurements. The membrane formula is depicted in Table S1.

2.3. Characterizations

The phase analysis of the hydrolyzed products of $SbCl_3$ was characterized by the X-ray diffraction (XRD, BRUKER). The laser microscope Raman spectrometer was used for substance composition analysis and structural identification (DXR, Thermo Fisher Scientific Inc., United States). The Fourier transform infrared (FT-IR) spectra were employed on the PVP, TA, and their mixture by a Bruker TENSOR II in the TR mode (Germen). X-ray photoelectron spectroscopy (XPS, Axis Ultra DLD, Kratos, England) was used to analysis the wire/25-3$SbCl_3$/TA3 membrane surfaces. Field emission scanning electron microscope (SEM) (FEI, Czech Republic) was used to obtain morphologies and element distributions of membranes. The optical images of the SDS stabilized emulsions before and after separation were recorded using the polarizing microscope (55XA, Shanghai GTX Semiconductor Co., Ltd). The rejection rate of SDS stabilized emulsion was calculated from the total organic carbon (TOC) of feed and filtration from the TOC analyzer (Shimadzu TOC-L, Japan). The contact angle instrument (JC2000D1, Shanghai Zhongchen Digital Technology Equipment Co., Ltd) measures the water or oil contact angles on the wire-mesh based oil–water membrane surfaces.

2.4. Evaluations of membrane properties

2.4.1. Water flux tests. The membrane was integrated into a custom-designed flux testing apparatus. 50 mL of deionized water to traverse the separation membrane was systematically recorded, and the flux was calculated as the average value of at least three times of measurements. The effective filtration area of the testing apparatus is 7 cm^2. The water flux across the separation membrane was quantitatively calculated using the following equation,

$$\text{Flux} = \frac{V}{A \times T} \quad (1)$$

where V represents the volume of water with the unit of L, A is the effective filtration area with the unit of m^2, and T is the filtration time with the unit of h.

The oil-in-water emulsion rejections (R, %) was calculated using eqn (2)

$$R = \frac{C_f - C_p}{C_f} \quad (2)$$

where C_p and C_f are the concentration of the permeate and feed solution, respectively.

2.4.2. Oil–water separation tests. The separation performances of the fabricated membrane were evaluated using a custom-built oil–water separation apparatus. A mixture comprising 25 mL of Sudan III-stained *n*-hexane and 25 mL of Evans blue-labeled aqueous solution was prepared. Furthermore, the surfactant stabilized oil-in-water emulsion was prepared with 0.9 g silicone oil, *n*-hexane, soybean oil or pump oil, 0.1 g of SDS and 1.0 L of deionized water stirring at 700 rpm for 24 h. 25 mL of emulsion was separated by the wire mesh-based membrane under gravity. This biphasic system was subsequently introduced into the separation chamber equipped with a 4 cm diameter membrane holder.

3. Results and discussion

3.1. Preparation of the wire mesh-based oil–water separation membranes

As shown in Fig. 1, the casting solution was dip-coated on the wire mesh, and it was immersed into the coagulation bath to obtain the wire mesh-based oil–water separation membranes. We separately added PVDF, PVP, and $SbCl_3$ in the casting solution, and TA in the coagulation bath. As a separation membrane modification material, the catechol polyphenol of TA could strengthen the interfacial bonding interactions with the metal mesh through multiple synergistic effects of hydrogen bonding, π–π stacking, and metal coordination, modulate the pore size of the separation membrane,[34,35] and improve the hydrophilic properties of the membrane surface *via* the high-density hydroxyl groups, which provides a natural and functionable green modification platform for the development of efficient and environmentally friendly separation membranes.[36] In addition, $SbCl_3$ was choose to added into the casting solution because it has a good dispersity in DMAC, provided abundant hydrophilic hydroxy groups to enhance surface hydrophilicity, and coordinated with TA.

Fig. 2a–f shows interactions between original materials during NIPS processes. The concentration of $SbCl_3$ was 15.6 mg mL^{-1}. The mass fractions of PVP, and TA were 0.2%, 3%, respectively. The pH of $SbCl_3$, PVP, and TA were 2.60, 3.35, and 3.15, and they were performed at 25 °C. The $SbCl_3$, PVP, and TA solutions were clear and transparent in Fig. 2a–c. The

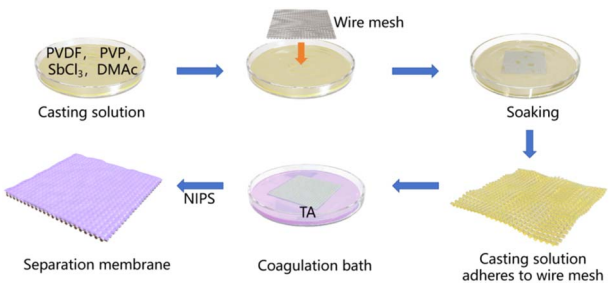

Fig. 1 The schematic diagram of the preparation processes of the wire mesh-based oil–water separation membrane.

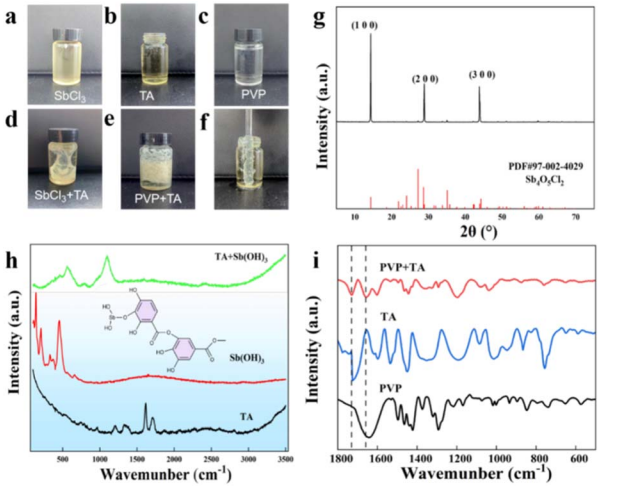

Fig. 2 Optical images of (a) $SbCl_3$ in DMAC, (b) PVP in DMAC, (c) TA in water, and the mixture of (d) $SbCl_3$ and TA, (e) PVP and TA, (f) the casting solution coated glass rod in TA solution. (g) The XRD pattern of the hydrolysis products of $SbCl_3$. (h) Raman spectra of TA, $Sb_4O_5Cl_2$, TA and $Sb_4O_5Cl_2$ mixture. $Sb_4O_5Cl_2$ powder was collected from the precipitants of 0.826 g of $SbCl_3$ in water, while TA and $Sb_4O_5Cl_2$ mixture were collected from the precipitants of $SbCl_3$ in TA solution. (i) FTIR spectra of PVP, TA, PVP and TA mixture. The mixture was the precipitate accumulated from (e).

instantaneous formation of a white gel upon mixing $SbCl_3$ and TA (Fig. 2d) indicates a rapid and strong coordination reaction, which is crucial for capturing TA during the fast NIPS process. To confirm the hydrolysis product, $SbCl_3$ was added into water to collect the precipitate the XRD characterization. From the XRD pattern in Fig. 2g, the red diffraction peaks are the standard diffraction peaks of $Sb_4O_5Cl_2$ (PDF#97-002-4029), and the black diffraction peaks above are the sample diffraction peaks. The diffraction peaks of the sample correspond to the characteristic peak positions of the $Sb_4O_5Cl_2$ standard card at the crystal planes (100), (200), and (300), indicating that the crystal structure of $Sb_4O_5Cl_2$ is the hydrolysis products of $SbCl_3$. The hydrolysis reaction is shown in eqn (3). Furthermore, 0.08 g and 1.652 g of $SbCl_3$ were separately added into water to collect the precipitants for XRD analysis. As shown in Fig. S1, the hydrolyzed product is Sb_2O_3 at low concentration of $SbCl_3$ (0.08 g) due to the completely hydrolysis, while it is $Sb_4O_5Cl_2$ at high concentration of $SbCl_3$. Although the hydrolysis products of different concentrations of $SbCl_3$ are different, all of them could release Sb^{3+} ions to form the metal polyphenol network with TA.

$$4SbCl_3 + 5H_2O = Sb_4O_5Cl_2\downarrow + 10HCl \quad (3)$$

The interaction between $Sb_4O_5Cl_2$ and TA was confirmed in the Raman spectra, as shown in Fig. 2h, the characteristic absorption peak of $Sb_4O_5Cl_2$ without forming coordination bonds is located at 450 cm^{-1}, while that of TA is at 1600 cm^{-1}. In the mixture, new strong peaks appear at 561 cm^{-1} and 1098 cm^{-1}, which are due to the formation of the Sb–O-cyclic benzene coordination bond between TA and $Sb_4O_5Cl_2$, and

C–O stretching vibration of phenolic groups in TA molecules coordinated with Sb^{3+} ions, respectively,[37] confirming the successful formation of the metal–polyphenol coordination. This rapid and strong coordination reaction is crucial for capturing TA during the fast NIPS process, and it is the pillar of our synergistic design. In addition, when $Sb_4O_5Cl_2$ interacts with TA, the vibration peaks also show a red-shift phenomenon, which further indicates the existence of a coordination interaction between TA and $Sb_4O_5Cl_2$.

The turbidity of the PVP/TA mixture (Fig. 2e) suggests the formation of an interpenetrating hydrogen-bonded network. The C=O group in PVP, which acts as a hydrogen-bond acceptor, and the phenolic hydroxyl groups in TA, which act as hydrogen-bond donors.[35,38] This interaction results in the formation of white flocculent substances and made the entire system turbid. Fig. 2i presents the FTIR spectra to confirm the hydrogen bond interactions between PVP and TA. In the FTIR spectrum of PVP, the absorption peak at 1642 cm^{-1} corresponds to the stretching vibration of the amide carbonyl group in PVP molecules. For the PVP/TA hybrid system, the absorption peak attributed to the stretching vibration of the amide carbonyl group in PVP shifts to 1656 cm^{-1}, attributing to the hydrogen bonding interaction between –C=O and –OH. Additionally, the carbonyl stretching vibration peak of TA moves from 1723 cm^{-1} to 1729 cm^{-1}, indicating that the interaction between the carbonyl group and hydrogen donors affects its vibrational activation energy. The FTIR results demonstrate that TA is successfully cross-linked with PVP through hydrogen bonding interactions. After dip-coating in the casting solution, the glass rod was immersed in the coagulation bath. As shown in Fig. 2f, a film was formed on the glass rod similar to the NIPS processes that conducted on the wire mesh. When the substrates including the wire mesh and glass rod coated with the casting solution immersed in the coagulation bath, the exchange of DMAC and water happened. Meanwhile, $SbCl_3$ hydrolyzed into $Sb_4O_5Cl_2$ clusters and coordinated with TA to form the metal–polyphenol network.[39–41] PVP segregated toward the interface of DMAC and water also interacted with TA *via* the hydrogen bond interactions. PVDF was precipitated from the system, and coated on the wire mesh substrates.

Fig. S2 shows the surface morphology of the original wire mesh, and it is smooth and clean. As shown in the low magnification of SEM image in Fig. 3, the membrane surfaces become rough as the NIPS happen on the wire mesh surfaces. The small pores on the surface of the wire mesh-based oil–water separation membrane can be clearly seen. As PVP from the casting solution diffused into TA solution with higher solubility, phase separation and leaching of PVP created micropores, and thus forming small pores on the membrane surfaces.[42] The Table S2 summarizes the pore information of the high magnification of SEM images using the software of Nano Measurer. The wire/25-raw/water membrane exhibits the largest average pore size and pore density. After addition of $SbCl_3$ in the casting solution or TA in the coagulation bath, the average pore size and pore density of the wire/25-3$SbCl_3$–water and wire/25-TA3 decrease as compared to these of the wire/25-raw/water membrane. The complex interactions change the phase separation, thereby influencing the pore structures. The thickness of the wire/25-3$SbCl_3$–TA3 membrane was 1.40 μm, which was characterized by the cross-sectional SEM image in Fig. S3.

The FTIR spectra of the wire mesh-based oil–water membranes are shown in the Fig. 4a. The characteristic peaks of the C–F bond are clearly observed at 600, 1179, and 1281 cm^{-1}, which is attributed to PVDF. The peak at 1401 cm^{-1} is the bending vibration of the $-CH_2$ bond, belonging to PVDF and PVP. Compared with the wire/25-raw/water membrane, the wire/25-3$SbCl_3$/water membrane exhibits new absorption peaks at 420 cm^{-1}, corresponding to the Sb–O stretching vibration.[43] Additionally, the wire/25-raw/TA3 membrane displays a new absorption peak at 1723 cm^{-1}, attributed to the C=O stretching vibration.[33] From the XPS spectra in Fig. S4, the C1s, N1s, O1s, Sb_3d, F1s, Fe2d peaks separately at 285, 400, 533, 557, 688, and 832 eV are displayed on the full spectra, respectively. The Sb–O, Sb–O–C, and Sb–Cl bonds are clearly shown in the Sb_3d peak of XPS in Fig. 4b. The Sb–O and Sb–Cl bonds belong to $Sb_4O_5Cl_2$, while the formation of the Sb–O–C bond indicates that $Sb_4O_5Cl_2$ reacts with TA *via* the metal–polyphenol coordination. As shown in Fig. 4c and d, the C1s of the wire/25-3$SbCl_3$/TA3 membrane can be divided into the C–F, C–O, C–N, and C–C bonds, while the O1s can be divided into the Sb–O, C=O, C–O, O–H bonds.

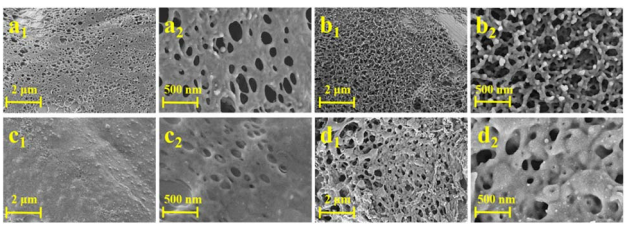

Fig. 3 The SEM images of the (a1, a2) wire/25-raw–water, (b1, b2) wire/25-3$SbCl_3$–water, (c1, c2) wire/25-TA3, (d1, d2) wire/25-3$SbCl_3$–TA3 membrane surfaces.

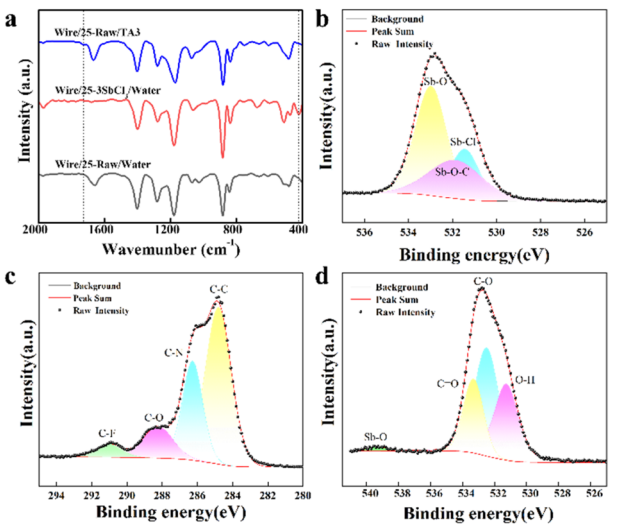

Fig. 4 (a) FTIR spectra of the wire mesh-based oil–water separation membranes. The (b) Sb_3d, (c) C1s, and (d) O1s peaks of XPS spectra of the wire/25-3$SbCl_3$/TA3 membrane surfaces.

3.2. Fluxes of the wire mesh-based oil–water separation membranes

The breakthrough height measurements are applied on the membranes using a tube with inner diameter of 8 mm. Membranes were primarily wetted by water to measure the breakthrough height of hexane. As shown in Fig. S5a, the wire/25-raw–water membrane exhibited a penetration height of 4.34 cm. Following modification with $SbCl_3$ or TA, the breakthrough height increased, and the wire/25-3$SbCl_3$–3TA membrane achieved a maximum penetration height of 49.4 cm. On the contrary, when water was using for the breakthrough height, membranes were primarily wetted by hexane, and the similar increased trend was shown in Fig. S5b. However, the wire/25-3$SbCl_3$–3TA membrane registered only 7.1 cm. These results unambiguously demonstrate that the synergistic coordination between $SbCl_3$ and TA substantially enhances the membrane liquid penetration resistance. The reinforcement arises from the formation of a dense and stable hydration layer on the membrane surface through cooperative coordination bonds and hydrogen bonding networks, which elevates the breakthrough pressure.

Since the mesh substrate is porous, the flux is highly improved in our work. Fig. 5a displayed the separation devices of the prepared membranes. An increase in the PVDF concentration has a significant impact on the membrane flux. As shown in Fig. 5b, as the addition amounts of the PVDF increased, the flux drops sharply from 109 000 L m^{-2} h^{-1} of the wire/20-3$SbCl_3$/TA5 membrane to 14 300 L m^{-2} h^{-1} of the wire/25-3$SbCl_3$/TA5 membrane, and finally plummets to 68 L m^{-2} h^{-1} of the wire/35-3$SbCl_3$/TA5 membrane. An increase in PVDF concentration elevates viscosity of the casting solution, leading to the delay of phase inversion, thereby forming a denser membrane structure.

Fig. 5c exhibited the relationship between the concentration of $SbCl_3$ and the flux. Without addition of $SbCl_3$, the flux of the wire/25-raw/TA3 membrane reaches to 12 000 L m^{-2} h^{-1}. When the amount of $SbCl_3$ in the casting solution is 0.08 g, the flux of wire/25-1$SbCl_3$/TA3 drops to 11 000 L m^{-2} h^{-1}. As the amount of $SbCl_3$ increased, the flux decreased. This systematic decline confirms that $SbCl_3$ concentration negatively impacts membrane permeability. SEM analysis revealed that $Sb_4O_5Cl_2$ hydrolyzed from $SbCl_3$ deposits progressively occluded membrane pores (Fig. 3c).

Fig. 5d shows the influence of TA on the water flux of the separation membrane. It was found that water flux decreased with the increased addition of TA in the coagulation bath. TA in the coagulation bath undergoes strong hydrogen bonding interactions with PVP in the casting solution, leading to the compact structure of the selective layer. Such a compacted structure increases the resistance for water molecules to pass through the membrane. As a result, the increase in mass transfer resistance or reduction in effective pore size, thus further reducing the membrane flux. The *in situ* formed hydrolysate and coordination complexes modulated the phase inversion kinetics and reduced the effective pore size of the selective layer, which is a trade-off for achieving superior separation efficiency. We have compared with values reported in recent literature for similar mesh-based membranes. Based on the comparison in the Table S3, the flux of our wire/25-3$SbCl_3$/TA3 membrane (8000 L m^{-2} h^{-1}) demonstrates not only competitive water flux, but also a simple and efficient preparation approach.

We further used the surfactant stabilized emulsion to test the separation performances. The feed emulsion was white color with poor transparency, and the emulsified pump oil droplets were obviously observed with the average diameter of 6.78 μm for the emulsified oil droplets in the optical microscope image in Fig. S6a. After separated by the wire/25-3$SbCl_3$/TA3 membrane, the filtration was transparent and clean, and no oil droplets could be seen in the optical microscope image in Fig. S6b, and the rejection rate was 99.1%, which was the average value of the three measurements, and calculated from the TOC results of the feed and filtration. We further used *n*-hexane, soybean oil, and silicone oil to prepare different kinds of emulsions, and their rejection rates were 99.5%, 98.8%, 96.7%, respectively, revealing the excellent rejection of the wire/25-3$SbCl_3$/TA3 membrane toward emulsions.

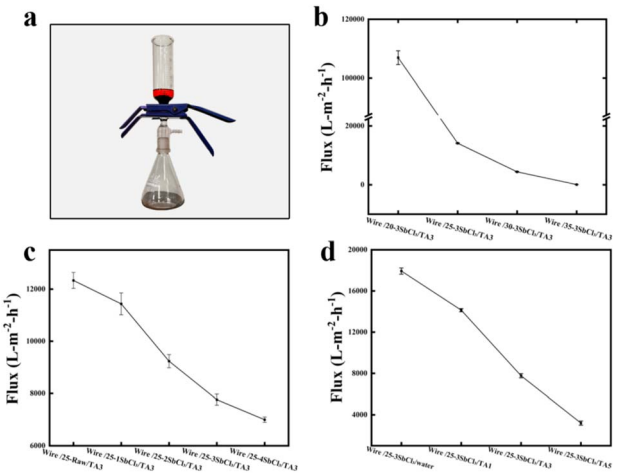

Fig. 5 (a) The image of the testing device. Water fluxes of the prepared wire mesh-based oil–water separation membranes with the varied concentrations of (b) PVDF, (c) $SbCl_3$, and (d) TA.

3.3. Surface wetting behavior of the wire mesh-based oil–water separation membranes

The contact angle, a crucial physical indicator of the interaction between liquid and solid surfaces, plays a significant role in the field of oil–water separation membranes to analyze the surface wetting behavior. As presented in Fig. S7a, the contact angle increased from 92.25° of the pristine wire mesh to 117.25° of the wire/25-raw/water membrane. The reduced hydrophilicity was due to the introduction of the hydrophobic PVDF matrix. As the concentration of $SbCl_3$ increased, the contact angle exhibited a decreasing trend. The contact angle of wire/25-5$SbCl_3$/water was measured at 40.75°, demonstrating a significant enhancement in hydrophilicity. This improvement is attributed to the formation of hydrophilic $Sb_4O_5Cl_2$ from the hydrolytic product

of $SbCl_3$ TA with the hydrophilic phenolic hydroxyl groups on the membrane surfaces also improved surface hydrophilicity. Fig. S7b illustrates the effects of varying TA concentration on the water contact angles on the separation membrane. As the TA concentration increased, a significant decrease in the contact angle was observed. Specifically, at a mass fraction of 5 wt% TA, the contact angle dropped to 11.5°, demonstrating a marked increase in hydrophilicity. The data in Fig. S7c show the effects of varying $SbCl_3$ concentrations, while Fig. S7d depicts the effect of changes in TA concentrations of the underwater oil contact angles on the membrane surfaces. In both cases, an increase in the concentration of either $SbCl_3$ or TA is accompanied by an elevation in the underwater oil contact angle. The addition of $SbCl_3$ and TA endowed the membrane surfaces with underwater superoleophobicity, indicating that water molecules strongly adhere on the membrane surface to form a hydration layer.

As shown in Fig. 6a, when the addition concentration of TA solution fixed at 3 wt%, the water contact angles of membranes were relatively minor changed as the $SbCl_3$ concentration increased. Fig. S8a and 6a exhibited the decrease of water contact angles for membranes as the increase of $SbCl_3$ concentration, but Fig. S8a shows a larger change in the contact angle. The main reason is that the coagulation bath of membranes in Fig. S8a is water, while that in Fig. 6a is 1 wt% TA. From the contact angle data, the change in the contact angle of the membrane surface by TA is greater than that by $SbCl_3$. Therefore, when compares the change of water contact angle as varying $SbCl_3$ concentration, the membranes which formed in the coagulation bath of water (Fig. S8a) is much larger than that of 1% TA (Fig. 6a). Conversely, when the addition amount of $SbCl_3$ was maintained 0.826 g in Fig. 6b, the water contact angle obviously decreased as the TA concentration increased. Fig. 6a and b reveals that variations in $SbCl_3$ and TA concentration significantly modulate the hydrophilicities of the separation membrane. Water contact angle (air–membrane interface) reveals the surface hydrophilicity, while underwater oil contact angle (oil–water interface) reveals the oil adhesion on the hydration layer. As shown in Fig. 6c and d, in addition of $SbCl_3$ and TA, all of the wire mesh-based membrane surfaces demonstrated underwater superoleophobicity with the underwater hexane contact angles over 150°. Due to the high surface energy of $Sb_4O_5Cl_2$ clusters and the abundance of phenolic hydroxyl groups in TA, each component individually enhanced the membrane's hydrophilicity.

Due to the convenience of the operation, dichloromethane was selected to measure the underwater oil sliding angle. As shown in Fig. S8a and b, the wire/25-raw–water, wire/25-3$SbCl_3$–water, wire/25-TA3, wire/25-3$SbCl_3$–TA3 membrane surfaces exhibited 90.0, 74.5, 5.3, and 2.5° of underwater oil sliding angles. For the wire/25-raw–water and wire/25-3$SbCl_3$–water membrane surfaces, oil droplets are almost adhered on the surfaces, while oil droplets easily roll off from the wire/25-TA3 and wire/25-3$SbCl_3$–TA3 membrane surfaces, indicating that TA plays an important role in changing the surface wetting behavior. The wire/25-3$SbCl_3$–TA3 membrane surface demonstrates a very low adhesion with the 2.5° of underwater oil sliding angle, which infers forming a dense hydration layer. Furthermore, the surface energy of the wire mesh, wire/25-raw–water, wire/25-3$SbCl_3$–water, wire/25-TA3, and wire/25-3$SbCl_3$–TA3 membranes is 23.0, 8.2, 73.9, 83.7, and 92.9 mJ m^{-2}, respectively, in Fig. S8e. Since PVDF contains the C–F bonds, the surface energy of the wire/25-raw–water membrane decreased. The addition of $SbCl_3$ and TA increases the surface energy of membranes, and the wire/25-3$SbCl_3$–TA3 membrane exhibited the highest surface energy among them. A higher surface energy enhances the adsorption capacity of water molecules on the membrane surface, thereby forming a denser hydration layer to resist foulants.

3.4. Self-cleaning performances of the wire/25-3$SbCl_3$/TA3 membrane

Fig. 7 vividly recorded the self-cleaning behavior of the wire/25-3$SbCl_3$/TA3 membrane. As depicted in Fig. 7a, pump oil stained with Sudan red was applied to the membrane, covering

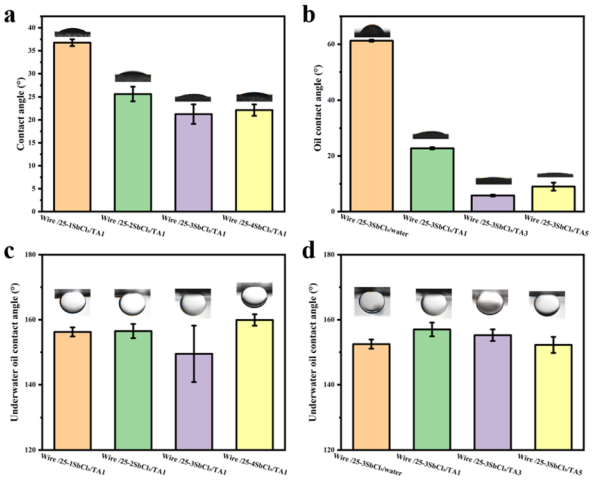

Fig. 6 (a and b) Water contact angles on the membrane surfaces. (c and d) Underwater oil contact angles on the membrane surfaces. The used oil was hexane.

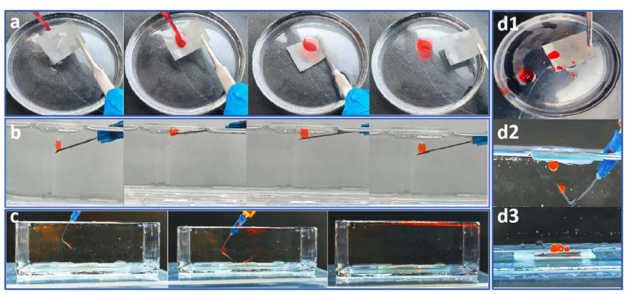

Fig. 7 (a–c) Self-cleaning behavior of the wire/25-3$SbCl_3$/TA3 membrane. (d1–d3) The comparison oil resistance of wire/25-raw/water membrane. (a, d1) The membrane was cut into 2 cm × 2 cm pieces and then thoroughly rinsed with deionized water before tests. (b, c, d2, d3) The membrane was cut into small pieces measuring approximately 2 cm × 2 cm and affixed to a slide using double-sided adhesive. Oil was dyed with Sudan red for better observation.

approximately two-thirds of its surface. Finally, the membrane was slowly immersed in deionized water, the oil droplet floated and left from the wire/25-3$SbCl_3$/TA3 membrane surface. The wire/25-3$SbCl_3$/TA3 membrane surface was clean and no pump oil residue was observed. In contrast, the wire/25-raw/water membrane surface without addition of $SbCl_3$ and TA, the membrane surface was polluted with oil residues in Fig. 7d1. Even after multiple rinsed with deionized water, a substantial amount of dyed pump oil residue retained on the membrane surface. As shown in Fig. 7b, when a dyed oil droplet was attached on the wire/25-3$SbCl_3$/TA3 membrane surface that immersed in water, the oil droplet remained on the point of the needle even though we put a pull on the oil droplet, displaying the low adhesion between oil and wetted wire/25-3$SbCl_3$/TA3 membrane surface. Compared to the same processes on the wire/25-raw/water membrane surface, the oil droplet was adhered on the wetted membrane surface. Moreover, when the wire/25-3$SbCl_3$/TA3 membrane sink to the bottom of the quartz trough, the oil droplets instantly bounced off the membrane surface in Fig. 7c. While the oil droplets aggregated on the wire/25-raw/water membrane surface in Fig. 7d3. As results, the wire/25-3$SbCl_3$/TA3 membrane exhibited the underwater self-cleaning property in water, while the wire/25-raw/water membrane surface displayed a strong underwater oil adhesion.

The simultaneous occurrence of hydrolysis, coordination, and hydrogen bonding interactions create a special wetting interpenetrating network on the wire mesh without destroying the substrate. The hydrolysis of $SbCl_3$ provides the reactive metal nodes of Sb^{3+}, and it reacted with TA to form the metal–polyphenol coordination. The hydrogen bonds between TA and PVP, along with the hydrophilic nature of all components, serve to swell the network and facilitate the formation of a dense and tightly bound hydration layer. The hydrated layer plays a critical role in enhancing the membrane's performance by significantly improving its surface hydrophilicity. As shown in Fig. 8, the hydrophilic groups provided from the TA, PVP and $Sb_4O_5Cl_2$ on the membrane surface exhibit a strong adhesion with water molecules, facilitating the formation of a stable hydration layer. This hydration layer acts as an effective barrier to prevent direct contact of oil droplets or other contaminants from the membrane surface, thereby substantially reducing the adsorption and deposition of contaminants on the membrane.[20,44,45] Therefore, the wire/25-4$SbCl_3$/TA3 membrane surface exhibited the excellent self-cleaning performances.

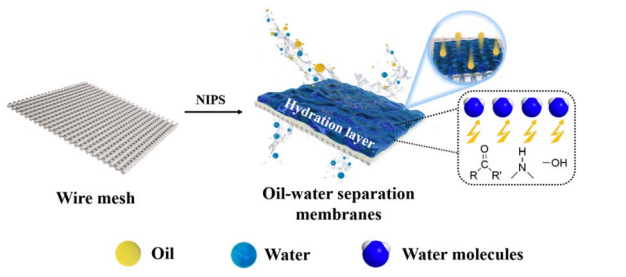

Fig. 8 Schematic illustration of the underwater self-cleaning mechanism of the separation membrane. The underwater oil repellency was on account of the formation of the hydration layer.

3.5. Stability of the wire/25-3$SbCl_3$/TA3 membrane

Stability investigation is necessary to understand the variations in separation performance under different pH and temperature conditions. In this study, acidic oil–water mixtures (0.012 mol L^{-1} HCl), alkaline oil–water mixtures (0.012 mol L^{-1} KOH), and neutral oil–water mixtures were prepared. These mixtures were heated to 50 °C or frozen to 10 °C, and separation tests were conducted with the wire/25-3$SbCl_3$/TA3 membrane, as illustrated in Fig. S9. The experimental results indicated that the wire/25-3$SbCl_3$/TA3 membrane successfully separated the oil–water mixtures at different pH values and temperatures, demonstrating robust stability in oil–water separation applications. As shown in Fig. S10, the wire/25-3$SbCl_3$–TA3 membrane could withstand the cross-cut for cycles. Fig. S11 shows the 10-cycle separation performance of the wire/25-3$SbCl_3$–TA3 membrane. The permeance of the wire/25-3$SbCl_3$–TA3 membrane remains basically stable throughout the 10-cycle filtration, with only minor variations. The surface morphology of the wire/25-3$SbCl_3$/TA3 membrane after 10-cycle was characterized by SEM in Fig. S12. The particle structure remained on the membrane surface structure remained particle structures, further revealing the long-term stability.

4. Conclusion

In summary, we have established a novel NIPS-enabled synchronous interaction strategy for functionalizing metal meshes. This strategy leverages the intrinsic dynamics of the phase separation process with the component hydrolysis, interfacial coordination, and hydrogen bonding interactions into a single step of membrane formation on the wire mesh, which is fundamentally different from conventional step-by-step approaches. During the NIPS processes, $SbCl_3$ in the casting solution hydrolyzed to $Sb_4O_5Cl_2$, and formed the Sb–O-cyclic benzene bonding with TA. Moreover, PVP in the casting solution also formed the hydrogen bonding with TA. The synergistic effect between $SbCl_3$, TA, and PVP provides a new design principle for constructing a hydration layer, effectively preventing oil foulants from the membrane surfaces. Furthermore, the wire/25-3$SbCl_3$/TA3 membrane exhibited remarkable stability in acidic and alkaline environments, cross-cut, or cycle filtration, making it well-suited for oil–water separation applications. The wire mesh-based oil–water separation membranes efficiently separate oil–water mixture solely under the influence of gravity, and achieving a flux of up to 8000 L m^{-2} h^{-1}. We anticipate this mechanism-inspired methodology will pave the way for developing next-generation advanced separation materials with high efficiency, durability, and scalability.

Data availability

Data will be available under request.

Supplementary information: The XRD pattern of the hydrolysis products; SEM images of pristine wire mesh; the cross-sectional SEM image of the Wire/25-3$SbCl_3$/TA3 membrane; full XPS spectra of the Wire/25-3$SbCl_3$/TA3 membrane surfaces; the height breakthrough of the Wire/25-Raw-water; optical microscope images and photos of the SDS stabilized oil-in-water emulsion before and after separation by the Wire/25-3$SbCl_3$/TA3 membrane; water contact angles, underwater oil angles and surface energy of varies samples; pH stability, abrasion, and 10-cycle filtration tests of the Wire/25-3$SbCl_3$/TA3 membrane; and the SEM image of the Wire/25-3$SbCl_3$/TA3 membrane after 10-cycle tests were shown in the supplementary file. See DOI: https://doi.org/10.1039/d5ra06305a.

Conflicts of interest

There is no conflict to declare.

Acknowledgements

The authors gratefully acknowledge financial support from the Innovation and Entrepreneurship project of Civil Aviation University of China for college students (IECAUC2025048). The authors extend their gratitude to Ms Xinao Han and Fanghui Wang from Scientific Compass (https://www.shiyanjia.com) for providing invaluable assistance with the data analysis.

Notes and references

1 X.-Y. Guo, L. Zhao, H.-N. Li, H.-C. Yang, J. Wu, H.-Q. Liang, C. Zhang and Z.-K. Xu, *Science*, 2024, **386**(6722), 654–659.
2 H. M. Mousa, H. S. Fahmy, G. A. M. Ali, H. N. Abdelhamid and M. Ateia, *Adv. Mater. Interfaces*, 2022, **9**(27), 2200557.
3 S. Peng, H. Ma, X. Hao, R. Han, X. Ji, L. Wang, Y. Fang, K. Pang, K. Il-Ho and X. Chen, *Environ. Res.*, 2024, **243**, 117777.
4 W. Meng, P. Li, Y. Lan, X. Shi, S. Peng, H. Qu and J. Xu, *Sep. Purif. Technol.*, 2020, **233**, 115988.
5 J. Gong, B. Xiang, Y. Sun and J. Li, *J. Mater. Chem. A*, 2023, **11**, 25093–25114.
6 M. Padaki, R. S. Murali, M. S. Abdullah, N. Misdan, A. Moslehyani, M. A. Kassim, N. Hilal and A. F. Ismail, *Desalination*, 2015, **357**, 197–207.
7 T. Xie, Y. Zhang, X. Zhang and Y.-X. Huang, *J. Membr. Sci.*, 2025, **723**, 123935.
8 H. Liang, A. Xie, Y. Qi, S. Yin, C. Wei, J. Luo, Y. Zhao, J. Cui and J. Pan, *Sep. Purif. Technol.*, 2024, **350**(18), 127987.
9 X. Zhang, C. Wang, X. Liu, J. Wang, C. Zhang and Y. Wen, *J. Cleaner Prod.*, 2018, **193**, 702–708.
10 X. Zhao, Y. Jiang, L. Cheng, Y. Lan, T. Wang, J. Pan and L. Liu, *Chin. Chem. Lett.*, 2022, **33**(8), 3859–3864.
11 G. Liu, Y. Cai, H. Yuan, J. Zhang, Z. Zhang and D. Zhao, *J. Membr. Sci.*, 2023, **668**, 121077.
12 E. Velayi and R. Norouzbeigi, *Surf. Coat. Technol.*, 2020, **385**, 125394.
13 Y. He, M. Liu, L. Zhai, H. Li, P. Song, X. Zhu and Y. Tang, *J. Environ. Chem. Eng.*, 2024, **12**(3), 112957.
14 W. Sun, L. Ding, P. Xu, B. Zhu, K. C. Ma and Q. Chen, *Water Environ. Res.*, 2025, **97**(1), e70006.
15 A. Matin, U. Baig, M. A. Gondal, S. Akhtar and S. M. Zubair, *J. Membr. Sci.*, 2018, **548**, 390–397.
16 S. Li, S. Xie, G. Chen, C. Zhang, K. Xiang and Z. Guo, *Sep. Purif. Technol.*, 2025, **359**, 130530.
17 K. Wang, T. C. Zhang, B. Wei, S. Chen, Y. Liang and S. Yuan, *Colloid Surf., A*, 2021, **608**, 125342.
18 Y. Xu, M. Liu, H. Li and A. Wali, *Surf. Coat. Technol.*, 2017, **325**, 661–672.
19 C.-T. Liu and Y.-L. Liu, *J. Mater. Chem. A*, 2016, **4**(35), 13543–13548.
20 W. Zheng, J. Huang, X. Zang, X. Xu, W. Cai, Z. Lin and Y. Lai, *Adv. Mater.*, 2022, **34**(42), 2204581.
21 J. Wang, F. Li, Y. Pan, F. Chen, C. Huang and X. Zhao, *Colloid Surf., A*, 2024, **701**, 134892.
22 N. Wen, X. Miao, X. Yang, M. Long, W. Deng, Q. Zhou and W. Deng, *Sep. Purif. Technol.*, 2018, **204**, 116–126.
23 G. Ren, Y. Song, X. Li, Y. Zhou, Z. Zhang and X. Zhu, *Appl. Surf. Sci.*, 2018, **428**, 520–525.
24 F. Chen, S. Hao, S. Huang and Y. Lu, *Powder Technol.*, 2020, **373**, 82–92.
25 M. Wang, J. Xu, W. Ren, J. Wang, Z. Zou and X. Wang, *Langmuir*, 2023, **39**(21), 7281–7293.
26 M. Nouri, M. T. Sadeghi, A. Rashidi and R. Norouzbeigi, *J. Pet. Explor. Prod. Technol.*, 2024, **14**, 1247–1258.
27 M. Paul, D. Upadhaya, D. D. Purkayastha and M. G. Krishna, *Appl. Surf. Sci.*, 2022, **583**, 152476.
28 T. Liu, J. P. Miao, L. L. Wang and Y. X. Hu, *Prog. Chem.*, 2023, **35**(8), 1199–1213.
29 D. M. Wang and J. Y. Lai, *Curr. Opin. Chem. Eng.*, 2013, **2**(2), 229–237.
30 M. Long, C. Yang, X. You, R. Zhang, J. Yuan, J. Guan, S. Zhang, H. Wu, N. A. Khan, R. Kasher and Z. Jiang, *J. Membr. Sci.*, 2021, **638**, 119689.
31 M. Long, Y. Jiang, C. Yang, Z. Xu, R. Zhang, J. Yuan, S. Zhang, M. Zhang, H. Wu and Z. Jiang, *Sep. Purif. Technol.*, 2023, **306**, 122743.
32 Z. Li, Y. Liu, X. Wei, Z. Zhang, F. Zhao, T. Wang, Y. Du, E. Shi, C. Fan, Y. Yang and Z. Jiang, *Adv. Funct. Mater.*, 2024, **34**, 2405915.
33 Z. Bai, K. Jia, S. Zhang, G. Lin, Y. Huang and X. Liu, *Adv. Funct. Mater.*, 2022, **32**(45), 2204612.
34 M. He, S. Zhang, Y. Su, R. Zhang, Y. Liu and Z. Jiang, *J. Membr. Sci.*, 2018, **556**, 285–292.
35 R. Zhang, M. He, D. Gao, Y. Liu, M. Wu, Z. Jiang, Y. Su and Z. Jiang, *J. Membr. Sci.*, 2018, **566**, 258–267.
36 M. Long, K. Chen, N. Khan, L. Yang, Y. Liu, D. An and H. Liu, *Colloid Surf., A.*, 2025, **726**, 138010.
37 Z. Sui, S. Hu, H. Chen, C. Gao, H. Su, A. Dai, Z. Wang, X. Zheng and Z. Zhang, *J. Mater. Chem. C*, 2017, **5**, 5451–5457.
38 Y. Wen, X. Yang, Y. Li, L. Yan, P. Sun and L. Shao, *Sep. Purif. Technol.*, 2024, **340**, 126775.
39 X. Zhang, Z. Fan, W. Xu, Q. Meng, C. Shen, G. Zhang and C. Gao, *J. Membr. Sci.*, 2023, **669**, 121330.
40 M. Qiu, Z. Shen, Q. Xia, X. Li, H. Huang, Y. Wang, Y. Liu and Y. Wang, *J. Colloid Interface Sci.*, 2022, **62**, 649–659.

41 F. Gang, C. Jonathan, R. R. Mariela, W. Pris and L. F. Ariel, *ACS Appl. Bio Mater.*, 2022, **5**(10), 4687–4695.
42 B. Vatsha, J. C. Ngila and R. M. Moutloali, *Phys. Chem. Earth*, 2014, **67**, 125–131.
43 Z. Sui, S. Hu, H. Chen, C. Gao, H. Su, A. Rahman, R. Dai, Z. Wang, X. Zheng and Z. Zhang, *J. Mater. Chem. C*, 2017, **5**(22), 5451–5457.
44 J. Gong, R. Jin, B. Xiang, F. Du, W. Liu and J. Li, *Sep. Purif. Technol.*, 2025, **360**(2(8)), 131013.
45 H. Liang, A. Xie, J. Chen, C. Wei, J. Luo, J. Cui and J. Pan, *Chem. Eng.*, 2025, **522**, 167572.